

Insights into Chromospheric Large-Scale Flows using Nobeyama 17 GHz Radio Observations

I. The Differential Rotation Profile

Srinjana Routh^{1,2}, Anshu Kumari^{3,4,*}, Vaibhav Pant¹, Jaydeep Kandekar⁵, Dipankar Banerjee^{6,7,8}, Mohd. Saleem Khan², and Dibya Kirti Mishra^{1,2}

¹ Aryabhata Research Institute of Observational Sciences, Nainital-263002, Uttarakhand, India

² Department of Applied Physics, Mahatma Jyotiba Phule Rohilkhand University, Bareilly-243006, Uttar Pradesh, India

³ Department of Physics, University of Helsinki, P.O. Box 64, FI-00014, Helsinki, Finland

⁴ Udaipur Solar Observatory, Physical Research Laboratory, Dewali, Badi Road, Udaipur-313 001, Rajasthan, India

⁵ Department of Physics, Ahmednagar College, Station Road, Ahilyanagar-414001, Maharashtra, India

⁶ Indian Institute of Space Science and technology, Valiamala, Thiruvananthapuram - 695 547, Kerala, India

⁷ Indian Institute of Astrophysics, Koramangala, Bangalore 560034, India

⁸ Center of Excellence in Space Sciences India, IISER Kolkata, Mohanpur 741246, West Bengal, India

July 4, 2025

ABSTRACT

Context. Although the differential rotation rate on the solar surface has long been studied using optical and extreme ultraviolet (EUV) observations, associating these measurements to specific atmospheric heights remains challenging due to the temperature-dependent emission of tracers observed in EUV wavelengths. Radio observations, being primarily influenced by coherent plasma processes and/or thermal bremsstrahlung, offer a more height-stable diagnostic and thus provide an independent means to test and validate rotational trends observed at other EUV wavelengths.

Aims. We aim to characterize the differential rotation profile of the upper chromosphere using cleaned solar full-disc 17 GHz radio imaging from the Nobeyama Radioheliograph (NoRH), spanning a little over two solar cycles (1992–2020).

Methods. A tracer-independent method based on automated image correlation was employed on daily full-disc 17 GHz radio maps. This method determines the angular velocities in 16 latitudinal bins of 15° each by maximizing the 2D cross-correlation of overlapping image segments.

Results. The best-fit parameters for the differential rotation profile are $A = 14.520 \pm 0.006^\circ/\text{day}$, $B = -1.443 \pm 0.099^\circ/\text{day}$, and $C = -0.433 \pm 0.267^\circ/\text{day}$. These results suggest that the upper chromosphere rotates significantly faster than the photosphere at all latitudes, with a relatively flatter latitudinal profile. A very weak anti-correlation ($\rho_s = -0.383$ (94.73%)) between the equatorial rotation rate and solar activity is also observed.

Conclusions. Our findings reaffirm the potential of radio observations to probe the dynamics of the solar chromosphere with reduced height ambiguity. The overlap of the equatorial rotation rate (A) found in this study with that for 304 Å in the EUV regime lends additional support to the view that the equatorial rotation rates increase with height above the photosphere. Future coordinated studies at wavelengths with better-constrained height formation will be crucial for further understanding the complex dynamics of the solar atmosphere.

Key words. plasmas – Sun: activity – Sun: chromosphere – Sun: general, Sun: radio radiation – Sun: rotation

1. Introduction

Large-scale flows on the Sun play a pivotal role in shaping the global dynamics of the solar atmosphere and influencing the distribution of magnetic fields across various layers of the solar interior and exterior. Among these, differential rotation, empirically formulated by Eq. (1), is one of the most fundamental and extensively studied global motions, observed not only at the solar surface but across the full extent of the solar atmosphere.

$$\Omega = A + B \sin^2 \theta + C \sin^4 \theta, \quad (1)$$

The differential rotation of the solar photosphere has been widely studied through techniques including feature tracking, flux modulation, and other methods (e.g., [Newton & Nunn 1951](#); [Snodgrass 1983](#)). Furthermore, recent advancements in helioseismology have significantly enhanced our understanding of the latitudinal and radial rotation profiles within the solar interior ([Antia et al.](#)

* Corresponding Author e-mail: anshu@pr1.res.in

1998; Antia et al. 2008). With growing observational capabilities spanning optical, Ultraviolet (UV), Extreme Ultraviolet (EUV), and radio wavelengths, the opportunity has emerged to reframe the problem in terms of a broader class of large-scale flows that pervade the atmosphere. From this perspective, differential rotation is not merely a parameterization of latitudinal shear, but a tracer of how angular momentum transport, plasma motions, and magnetic fields are coupled across spatial and temporal scales in the solar atmosphere.

However, despite centuries of investigation, the nature of how such flows evolve with height and temperature, and their inter-connection across stratified atmospheric layers, remains incompletely understood due to the height ambiguity of tracers involved in the extraction of the differential rotation profile. Recent studies, particularly using the Atmospheric Imaging Assembly (AIA) onboard the Solar Dynamic Observatory (SDO; e.g., Sharma et al. 2020; Routh et al. 2024), have demonstrated that a possible connection between the rotation rate of the solar atmosphere might exist with height above the photosphere. These trends suggest that the atmospheric layers are not passively rotating but may be dynamically linked to deeper processes, possibly governed by the magnetic field topology. This line of reasoning has found support in works that compare atmospheric rotation with internal rotation profiles derived from helioseismology (e.g., Badalyan 2010; Finley & Brun 2023), hinting at connections mediated by magnetically anchored structures.

Despite such broad efforts, the phenomenon of differential rotation has been difficult to grasp in the upper and hotter solar atmosphere due to various reasons, including but not limited to the fast-changing nature of higher atmospheric tracers as well as the height ascribed to them. Although the faster rotation of the hotter solar atmosphere, specifically the chromosphere, has long been suggested through different methods and different datasets (Livingston 1969; Mishra et al. 2024; Routh et al. 2024), an ambiguity in the exact height of the origin of the emission dataset in such studies has always left a gap to be fulfilled. Extending this inquiry into radio wavelengths offers an even less ambiguous insight into the chromosphere, transition region and corona. Radio observations, such as those from the Nobeyama Radioheliograph (NoRH), provide height-stable diagnostics of the upper chromosphere and transition region (e.g., 34 and 17 GHz emission (8.8 and 17.6 mm, respectively); Selhorst et al. 2008), thereby avoiding the temperature-based ambiguities that often affect EUV diagnostics. In an attempt to address this gap, this study utilizes a tracer-independent method to ascertain the spatial and temporal variation in the differential rotation of the solar atmosphere at well-defined heights above the photosphere as determined from radio emission. The article is arranged as follows: section 2 discusses the observations and data analysis method, section 3 discusses the results. Finally, section 4 summarizes the present work and discusses the conclusion.

2. Observation and data analysis

2.1. The Nobeyama Radioheliograph

The Nobeyama Radioheliograph, operational since 1992 July till 2020 March, has been observing the Solar chromosphere and the transition region at frequencies of 34 and 17 GHz, respectively at a resolution of 10" (Nakajima et al. 1994). The cleaned solar full-disc images¹ that are used in this study have dimensions of 512×512 pixel² with a pixel scale of 4.91". These images are image registered and aligned such that the solar north coincides with the image north.

2.2. Data pre-processing and method of image correlation

Since the cleaned solar full-disc fits image data from the Nobeyama Radioheliograph primarily represents the brightness temperature of various features in the solar atmosphere, the maximum brightness temperature values in the dataset can vary significantly depending on the observed solar activities (Selhorst et al. 2003). This might create an issue when the method of image correlation, which primarily utilizes the intensity gradient information to minimize the brightness conservation or the optical flow equation (Neggers et al. 2016). To get rid of this spuriousness in the data, the entire dataset is first minmax-scaled (see Fig. 1b), such that the scaled brightness of each pixel i in the dataset is given by the following equation,

$$B_{i,scaled} = \frac{B_i - B_{min}}{B_{max} - B_{min}} \quad (2)$$

where, B_{min} and B_{max} are the minimum and maximum brightness of the entire dataset. This step ensures the entire dataset has brightness values $\in [0, 1]$, thereby standardizing the dataset. The resulting dataset is then subjected to the method of image correlation similar to as outlined in Mishra et al. (2024) and Routh et al. (2024) to obtain the sidereal rotation rate (Ω_θ), corresponding to the maximum correlation coefficient in each latitudinal bin. A brief description of the method is discussed in Appendix A.

3. Results and discussion

After setting a threshold on the value of cross-correlation coefficient (C.C.) to ensure the integrity of the analysis statistics (a detailed discussion of this approach and further examination of this technique is available in Mishra et al. (2024); Routh et al. (2024)), an average Ω_θ , weighted by the corresponding C.C. in each latitudinal bin is obtained for each latitude θ . The uncertainty of these values is then determined as a combination of the standard statistical error (σ_{SSE}) and the least count error². These values are subsequently fitted to Eq. (1) using Levenberg-Marquardt least square (LMLS; Markwardt 2009) method to obtain the best-fit parameters A , B and C and the respective uncertainty (ΔA , ΔB and ΔC) in determining them. Thereafter, we obtain the values $A + \Delta A = 14.520 \pm 0.006$

¹ <https://solar.nro.nao.ac.jp/norh/images/daily/>

² $\sigma_{LCE} = 0.1^\circ$

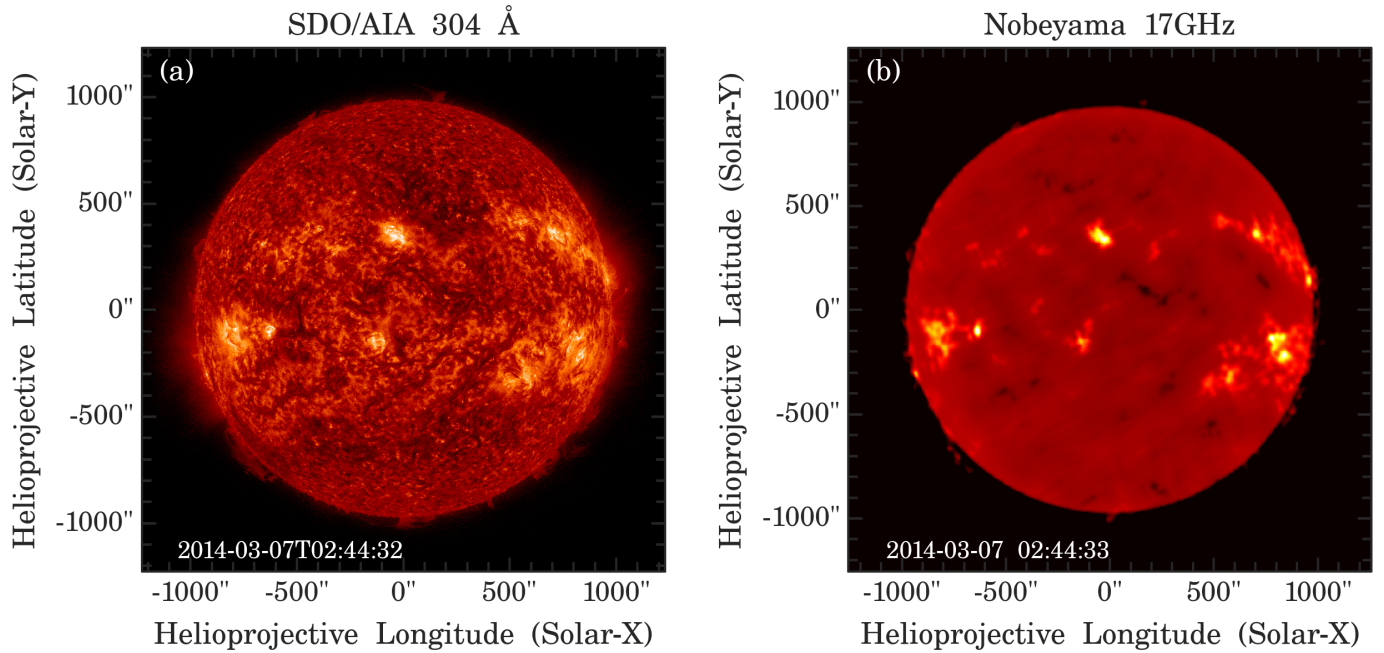


Fig. 1. The Sun from (a) a space-based perspective as seen by the Atmospheric Imaging Assembly (AIA) atop the Solar Dynamic Observatory and (b) a ground-based perspective as seen by the Nobeyama Radioheliograph.

$^{\circ}/\text{day}$, $B + \Delta B = -1.443 \pm 0.099 ^{\circ}/\text{day}$ and $C + \Delta C = -0.433 \pm 0.267 ^{\circ}/\text{day}$ (Fig. 2) for the solar chromosphere as seen at a frequency of 17 GHz.

Upon examining Fig. 2, it is immediately apparent that the rotational profile is significantly higher than that of the photospheric plasma and sunspot groups, and it is relatively flatter, indicating that the solar chromosphere at a height of 3000 ± 500 km above the solar visible surface rotates more rapidly than the underlying photosphere at all latitudes, similar to findings by Chandra et al. (2009) using three years of NoRH data. It is also evident that the rotational profile displays a relatively flatter trend, suggesting a reduced differential nature. This result aligns well with the rotational profile of the chromosphere from SDO/AIA 304 Å (Routh et al. 2024), which samples plasma in the temperature range of $\log_{10} T = 4.7$ K (Lemen et al. 2012) and supposedly represents a height of 2820 ± 400 km (Kwon et al. 2010) above the photosphere. Additionally, these findings are consistent with several studies such as Li et al. (2020); Mishra et al. (2024) that utilized spectroheliogram data from both space and ground-based data probing different parts of the solar chromosphere. The results for A obtained in this study also conform to the existing trend for equatorial rotation rate at different heights in the solar atmosphere, as suggested by previous studies, as shown in Fig. 3.

Next, we look at the variation of the rotational parameters with respect to the strength of the solar cycle, as designated by sunspot number (SSN). From a correlation analyses involving the Spearman correlation coefficient (ρ_s) to explore any potential monotonous relationship, we find that both the equatorial rotation rate (A) and the latitudinal gradient (B) exhibit little to no significant relationship with solar activity (Fig. 4). This observation is consistent with previous studies similar to Bertello et al. (2020); Mishra et al. (2024); Routh et al. (2024). However, upon closer inspection, a very weak negative correlation for A ($\rho_s = -0.4$ (94.72%)) with solar activity strength is observed, aligning with Brajša et al. (2006); Li et al. (2023), but no such relationship is evident for B ($\rho_s = -0.11$ (39.25%)).

4. Summary & conclusions

We analyzed 28 years of radio imaging data from the Nobeyama Radio Observatory to examine the differential rotation profile of the upper chromosphere using an automated image correlation technique³. The distinguishing factor of this method is in the fact that unlike the tracer method which depends heavily on the availability of a singular feature distinguished by intensity, the method of image correlation is sensitive to only intensity gradients in each pixel and does not depend heavily on the availability of dominant features. This ensures that even during minima periods, a proper shift is identified based only on the intensities of each pixel in a bin. However, this also allows for the rotational profiles of several prominent features like coronal holes, filaments and active regions to coexist, without being differentiated. A numerical analysis to differentiate the contribution of these features may be attempted in the future, but remains out of scope for this particular study. Our goal in this study was to associate the derived rotational profile with a specific height in the upper solar atmosphere, reducing the ambiguity often encountered with EUV observations, which are typically sensitive to particular temperatures, leading to greater uncertainty regarding the representative height above the photosphere as higher atmospheric features of similar temperature range may also contribute to the filter-recorded intensity. Our findings indicate that the solar atmosphere at a height of 3000 ± 500 km rotates significantly faster than the photosphere below and shares similar rotational characteristics with 304 Å from SDO/AIA. This agreement of parameters obtained from a temperature

³ The generalized code is available for open source use at : <https://github.com/srinjana-routh/Image-Correlation>

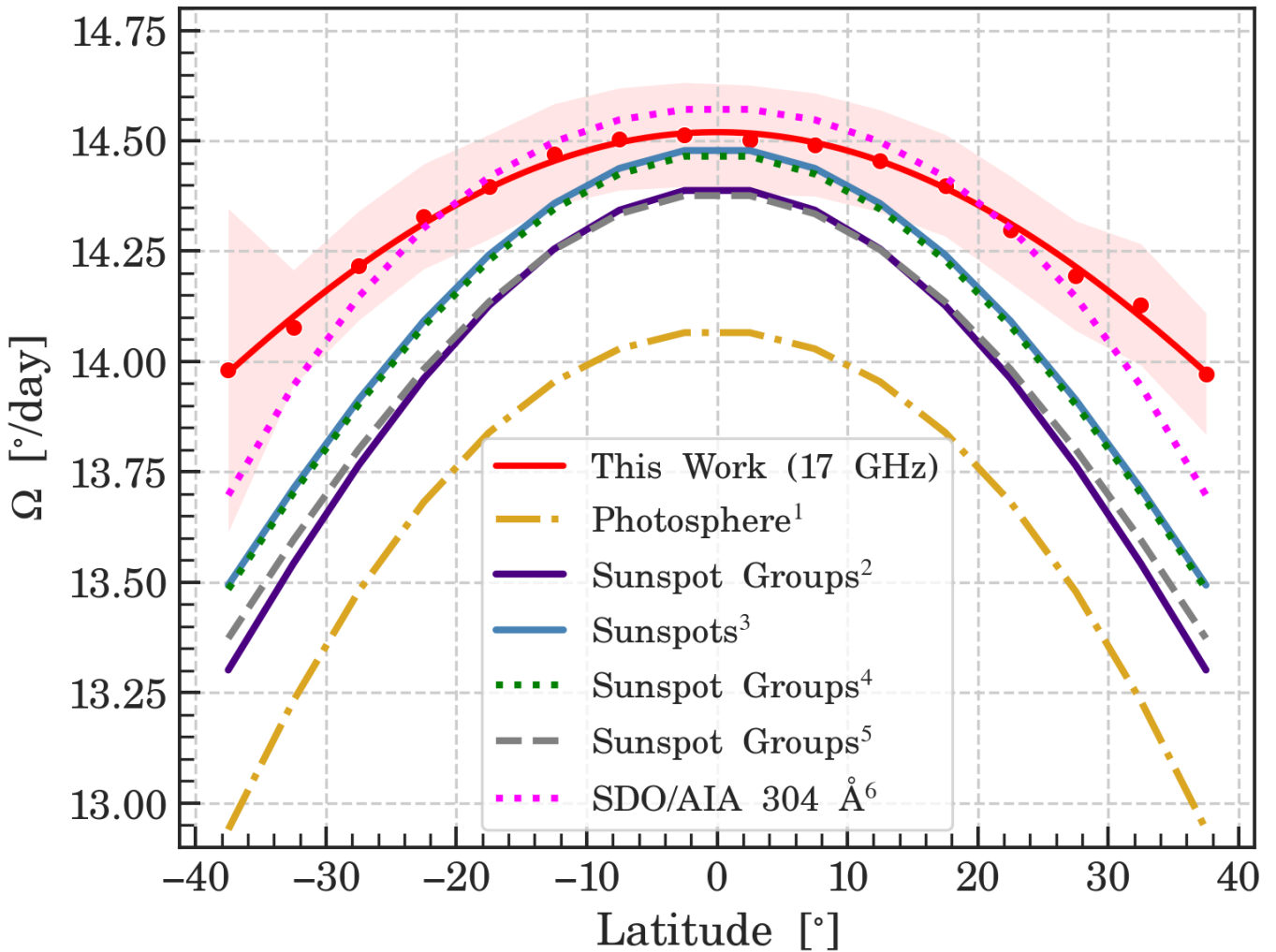


Fig. 2. Rotation profile of solar chromosphere as obtained from 17 GHz data from Nobeyama Radioheliograph data, when compared with rotational profiles from ¹Snodgrass (1983, 1984), ²Howard et al. (1984), ³Poljančič Beljan et al. (2017), ⁴Ruždjak et al. (2017), ⁵Jha et al. (2021) and ⁶Routh et al. (2024).

sensitive channel which can include contributions from features at different heights reaching $\log_{10}T = 4.7$ K locally, is within the 3σ range (Fig. 3) with values derived from radio emissions, which predominantly originate from a single height (Selhorst et al. 2008; Oliveira e Silva et al. 2016). Such an agreement reduces ambiguity in the possibility that a genuine upward trend in the solar atmosphere with increasing height. It is also worth noting that the overlap of the equatorial rotation rate (A) found in this study with that for 304 Å, which in turn matches the A obtained for a depth of $r = 0.94R_{\odot}$ (Routh et al. 2024), may further support the idea that magnetic features in the higher solar atmosphere have footpoints deep into the convection zone (e.g., Weber (1969); Mancuso et al. (2020) and references therein).

An investigation into the impact of solar activity strength on the parameters A and B revealed that neither parameter is significantly affected, although a very weak negative correlation was observed for A , in agreement with Li et al. (2013); Jurdana-Šepić et al. (2011); Ruždjak et al. (2017); Wan & Gao (2022). This result may be understood in light of the numerical simulations explored by Brun (2004); Brun et al. (2004), whose results suggest that a subtle deceleration in differential rotation may be attributed to Maxwell stresses opposing Reynolds stresses, leading to reduced differential rotation. A similar result was obtained analytically by Lanza (2006, 2007) for young late-type stars. However, this inference should be taken with caution, as the correlation coefficient and its confidence level are too weak to draw any definitive conclusions.

This study's findings contribute to our understanding of the complex relationship between solar rotation and atmospheric height, by decreasing the ambiguity associated with the representative height associated with the observed rotational profile of higher solar atmosphere that has long been explored using optical, UV and EUV wavelengths. Further studies exploring coronal counterparts in wavelengths where height determination is less ambiguous could provide stronger confidence in the trend of rotation rate so consistently observed and thereby explore the mechanisms behind the observed rotational characteristics and their implications for solar dynamics. Additionally, long-term monitoring of these parameters could provide insights into potential changes in solar rotation over extended periods and as to why barely any impact of solar activity is seen on the chromospheric rotational rate, which may have further implications for solar activity cycles and space weather predictions.

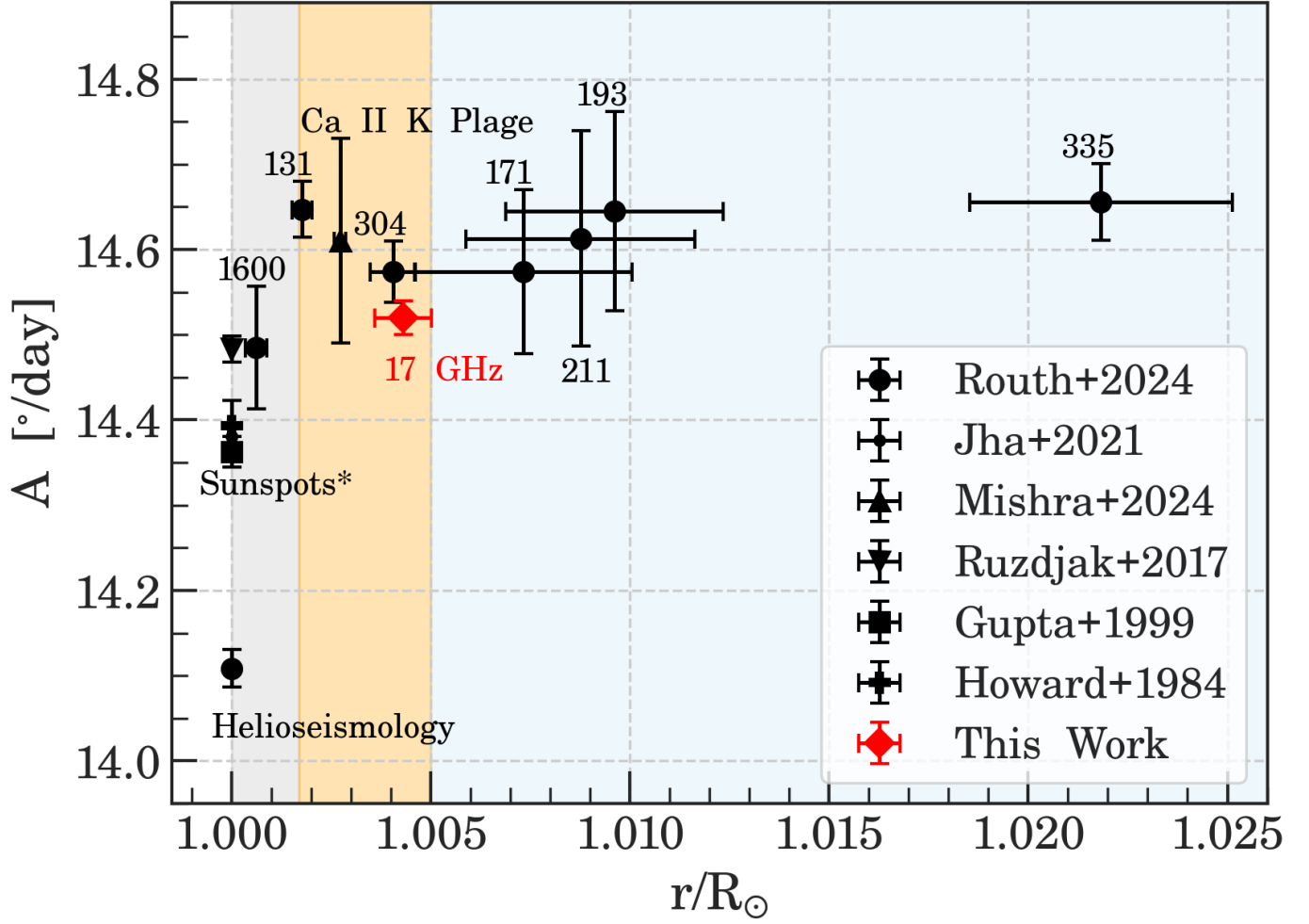


Fig. 3. Variation in quatorial rotation rate from photosphere to different parts of corona from recent works. The umbrella label of "sunspots" is demarcated with an asterisk (*) to indicate different datasets used by different studies (see [Appendix B](#)). Extents of different layers of the solar atmosphere are shaded differently (photosphere in gray, chromosphere in gold, and corona in light blue) to allow distinction between the same. The heights representing the different temperature sensitive filters have been taken from [Sanjay et al. \(2024\)](#) (for 131 Å only) and the references in [Routh et al. \(2024\)](#). The representative height for 17 GHz has been obtained from [Zirin \(1988\)](#). The errorbars along y represent 3σ variation in the parameters, while along x the errorbars represent the exact variation reported in the mentioned studies. A detailed table compiling all values in this figure and several other studies are available for reference in [Appendix B](#).

Acknowledgements. S.R. is supported by funding from the Department of Science and Technology (DST), Government of India, through the Aryabhata Research Institute of Observational Sciences (ARIES). The computational resources utilized in this study were provided by ARIES. AK acknowledges the ANRF Prime Minister Early Career Research Grant (PM ECRG) program. The data utilized in this work has been acquired from the Nobeyama Radio Observatory (NRO) database. All the authors are grateful to the observers at NRO for the data. Yearly mean sunspot numbers come from the source: WDC- SILSO, Royal Observatory of Belgium, Brussels, and these can be downloaded from <https://www.sidc.be/silso/>.

References

- Antia, H. M., Basu, S., & Chitre, S. M. 1998, *Monthly Notices of the Royal Astronomical Society*, 298, 543
 Antia, H. M., Basu, S., & Chitre, S. M. 2008, *ApJ*, 681, 680
 Badalyan, O. G. 2010, *New Astronomy*, 15, 135
 Balthasar, H., Vazquez, M., & Woehl, H. 1986, *A&A*, 155, 87
 Bertello, L., Pevtsov, A. A., & Ulrich, R. K. 2020, *ApJ*, 897, 181
 Brajša, R., Ruždjak, D., & Wöhl, H. 2006, *Sol. Phys.*, 237, 365
 Brun, A. S. 2004, *Sol. Phys.*, 220, 333
 Brun, A. S., Miesch, M. S., & Toomre, J. 2004, *ApJ*, 614, 1073
 Chandra, S., Vats, H. O., & Iyer, K. N. 2009, *MNRAS*, 400, L34
 Chatterjee, S., Banerjee, D., & Ravindra, B. 2016, *The Astrophysical Journal*, 827, 87
 Finley, A. J. & Brun, A. S. 2023, *A&A*, 679, A29
 Gupta, S. S., Sivaraman, K. R., & Howard, R. F. 1999, *Sol. Phys.*, 188, 225
 Howard, R., Gilman, P. I., & Gilman, P. A. 1984, *ApJ*, 283, 373
 Howard, R. F., Gupta, S., & Sivaraman, K. 1999, *Solar Physics*, 186, 25
 Jha, B. K., Priyadarshi, A., Mandal, S., Chatterjee, S., & Banerjee, D. 2021, *Sol. Phys.*, 296, 25

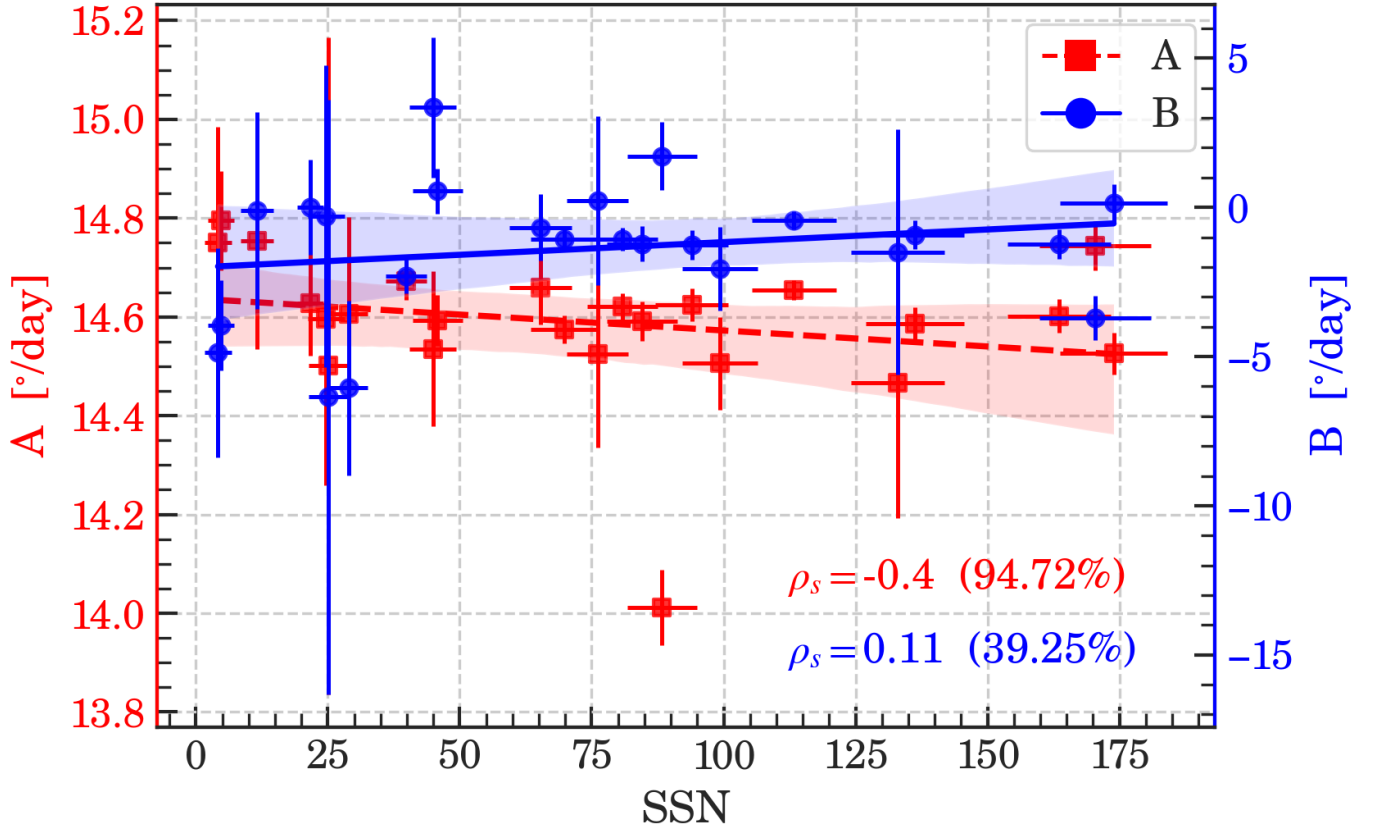


Fig. 4. Correlation plot of equatorial rotation rate (A; in red) and latitudinal gradient (B; in blue) with yearly sunspot number and their error estimate in y and x directions, respectively. The lines of best fit are exhibited to visualize the generalized trend in the correlation. The shaded regions with each line correspond to the confidence interval of the fit.

- Jurdana-Šepić, R., Brajša, R., Wöhl, H., et al. 2011, *A&A*, 534, A17
 Kwon, R.-Y., Chae, J., & Zhang, J. 2010, *The Astrophysical Journal*, 714, 130
 Lanza, A. F. 2006, *MNRAS*, 373, 819
 Lanza, A. F. 2007, *A&A*, 471, 1011
 Lemen, J. R., Title, A. M., Akin, D. J., et al. 2012, *Solar Physics*, 275, 17
 Li, K., Shi, X. J., Xie, J., et al. 2013, *Monthly Notices of the Royal Astronomical Society*, 433, 521
 Li, K. J., Wan, M., & Feng, W. 2023, *MNRAS*, 520, 5928
 Li, K. J., Xu, J. C., Xie, J. L., & Feng, W. 2020, *The Astrophysical Journal Letters*, 905, L11
 Livingston, W. C. 1969, *Solar Physics*, 9, 448
 Mancuso, S., Giordano, S., Barghini, D., & Telloni, D. 2020, *A&A*, 644
 Markwardt, C. B. 2009, in *Astronomical Society of the Pacific Conference Series*, Vol. 411, *Astronomical Data Analysis Software and Systems XVIII*, ed. D. A. Bohlender, D. Durand, & P. Dowler, 251
 Mishra, D. K., Routh, S., Jha, B. K., et al. 2024, *The Astrophysical Journal*, 961, 40
 Nakajima, H., Nishio, M., Enome, S., et al. 1994, *IEEE Proceedings*, 82, 705
 Neggers, J., Blaysat, B., Hoefnagels, J. J., & Geers, M. M. 2016, *International Journal for Numerical Methods in Engineering*, 105, 243
 Newton, H. W. & Nunn, M. L. 1951, *Monthly Notices of the Royal Astronomical Society*, 111, 413
 Oliveira e Silva, A. J., Selhorst, C. L., Simões, P. J. A., & Giménez de Castro, C. G. 2016, *A&A*, 592, A91
 Poljančič Beljan, I., Jurdana-Šepić, R., Brajša, R., et al. 2017, *Astronomy & astrophysics*, 606, A72
 Routh, S., Jha, B. K., Mishra, D. K., et al. 2024, *ApJ*, 975, 158
 Roša, D., Brajša, R., Vršnak, B., & Wöhl, H. 1995, *Sol. Phys.*, 159, 393
 Ruždjak, D., Brajša, R., Sudar, D., Skokić, I., & Poljančič Beljan, I. 2017, *Sol. Phys.*, 292, 179
 Ruždjak, D., Ruždjak, V., Brajša, R., & Wöhl, H. 2004, *Sol. Phys.*, 221, 225
 Sanjay, Y., Krishna Prasad, S., Erdélyi, R., et al. 2024, *ApJ*, 975, 236
 Selhorst, C. L., Silva, A. V. R., Costa, J. E. R., & Shibasaki, K. 2003, *A&A*, 401, 1143
 Selhorst, C. L., Silva-Válho, A., & Costa, J. E. R. 2008, *A&A*, 488, 1079
 Sharma, J., Kumar, B., Malik, A. K., & Vats, H. O. 2020, *Monthly Notices of the Royal Astronomical Society*, 492, 5391
 Skokić, I., Brajša, R., Roša, D., Hržina, D., & Wöhl, H. 2014, *Sol. Phys.*, 289, 1471
 Snodgrass, H. B. 1983, *ApJ*, 270, 288
 Snodgrass, H. B. 1984, *Sol. Phys.*, 94, 13
 Sudar, D., Brajša, R., Skokić, I., & Benz, A. O. 2019, *Solar physics*, 294, 163
 Wan, M. & Gao, P.-x. 2022, *ApJ*, 939, 111
 Weber, E. J. 1969, *SoPh*, 9, 150
 Wittmann, A. D. 1996, *Sol. Phys.*, 168, 211
 Zirin, H. 1988, *Astrophysics of the Sun* (Cambridge University Press)

Appendix A: Segmentation and correlation analysis of the radio images

Appendix A.1: Method of image correlation

At a time a single pair of images, temporally separated by a day ($\Delta t \leq 1$), are studied. These pair of images are first projected onto the heliographic grid 1800×1800 in dimension (0.1° along longitude and latitude; see Fig. A.1a and b). The result is then

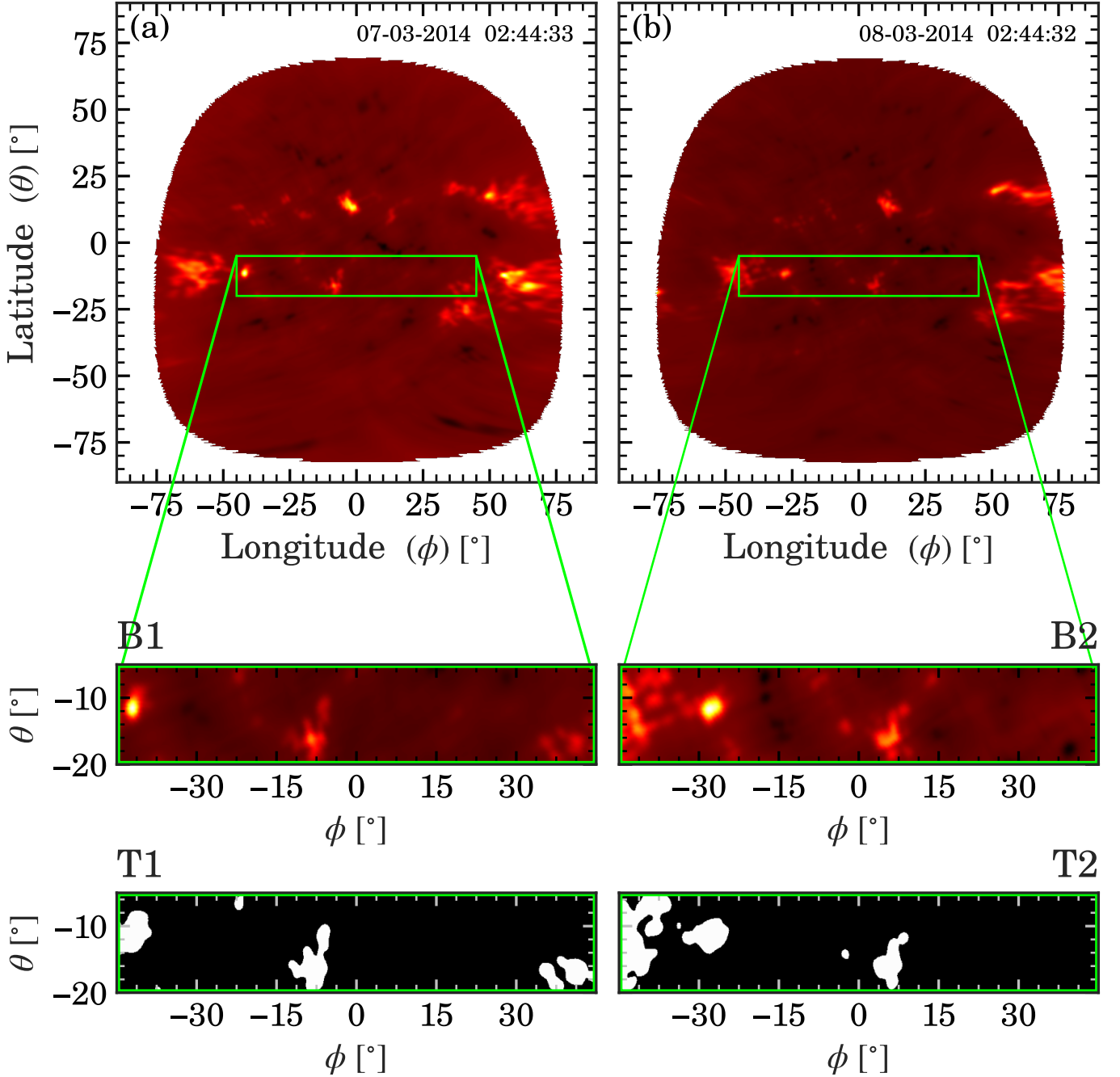


Fig. A.1. Set of images on (a) 7th March, 2014 and (b) 8th March, 2014 from the Nobeyama dataset after the conversion to Stonyhurst heliographic coordinates. Green rectangular boxes depict the bins B1 and B2, extending from -20° to -5° in latitude and $\pm 45^\circ$ in longitude each, on which image correlation is applied. The bins T1 and T2 depict the dominant bright features in the same bins that are majorly contributing to the correlation as demonstrated by adaptive intensity thresholding.

divided in 16 overlapping bins of size 15° and stride of 5° in the latitudinal direction, spanning $\pm 45^\circ$ in latitude. Since there exists a center-to-limb variation in intensity which might affect our measurement of the longitudinal shift, the longitudinal span of these bins were restricted to $\pm 45^\circ$, thereby close to the disc centre where the effects of centre-to-limb variation is minimal (see for e.g., Sudar et al. (2019) and references therein). At a time, bins of the same latitudinal extent temporally separated by 1 day (B1 and B2 in Fig. A.1) are subjected to the method of image correlation. In this method, one bin is shifted with respect to the other bin within

[[h!]]

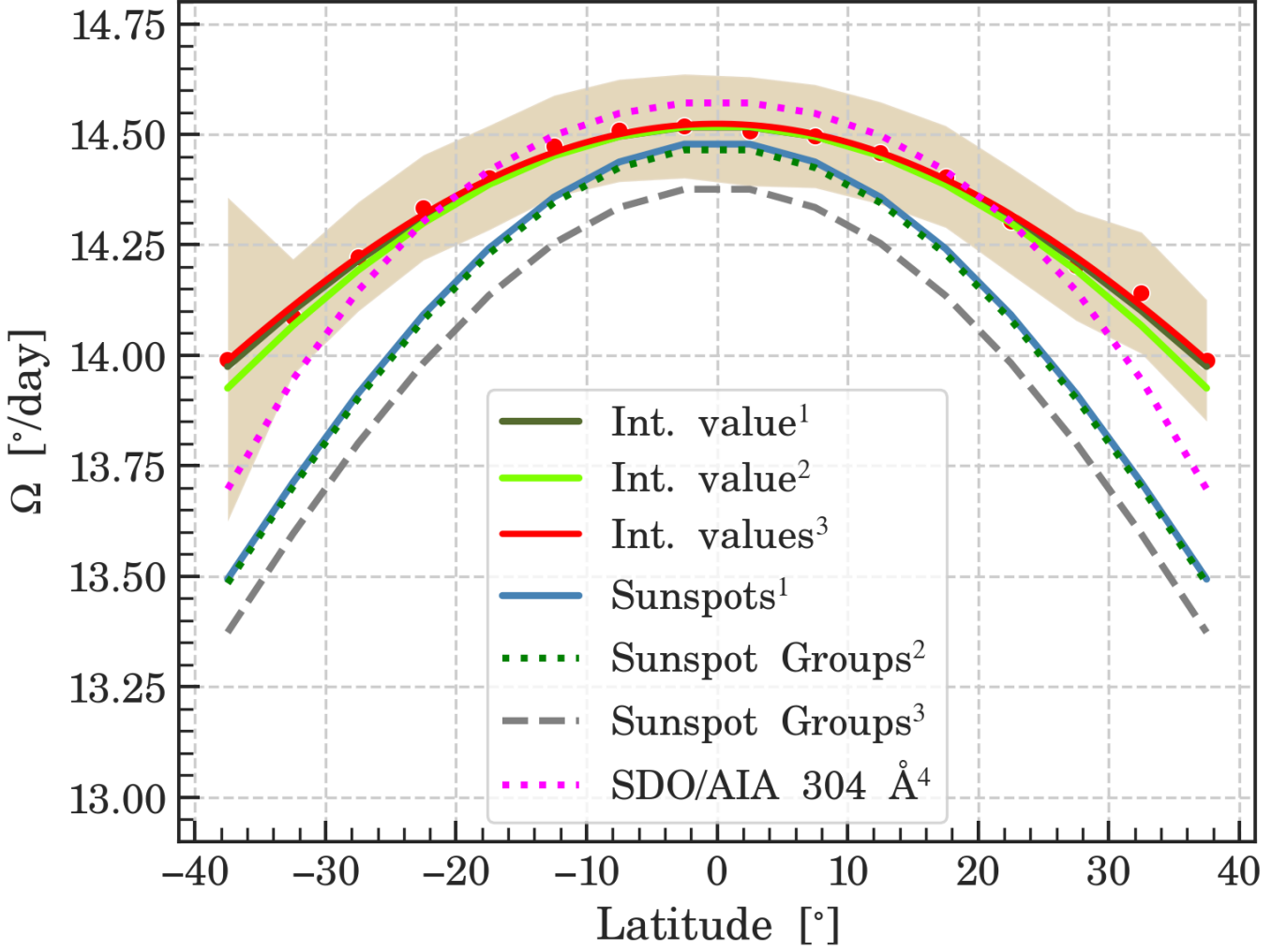


Fig. A.2. Obtained rotational profiles for Nobeyama 17 GHz data for different initial values from ¹Ruždjak et al. (2017) and ²Poljančič Beljan et al. (2017) along with the result from the initial values taken from ³Jha et al. (2021), as discussed in the main text, compared with the values from ⁴Routh et al. (2024). The shaded region of each colour for initial guesses denotes the error pertained in the individual values for each case, as discussed in section 3.

the range of $\Delta\phi \in \Delta\phi_0 \pm 3^\circ$ and $\Delta\theta \in \Delta\theta_0 \pm 1^\circ$ in longitudinal and latitudinal directions, respectively⁴. The initial guesses ($\Delta\theta_0, \Delta\phi_0$) were calculated from the rotation rate of sunspot groups (Jha et al. 2021). An analysis locating the maximum of the resulting 2D correlation coefficient gives the value of the longitudinal shift ($\Delta\phi$), as dictated by the dominant features, when present in the given latitudinal bin (see T1 and T2 in Fig. A.1; the method of segmentation of these features are discussed in subsection A.1). This value is then utilized to obtain the synodic value of Ω ($\Omega_\theta^{\text{syn}} = \frac{\Delta\phi}{\Delta t}$) at the mid-latitude θ_m of the same latitudinal bin. To incorporate the effect of the motion of the Earth around the Sun, we apply the sidereal correction (Roša et al. 1995; Wittmann 1996; Skokić et al. 2014; Mishra et al. 2024) on the synodic rotation rate to get the sidereal rotation rate (Ω_θ), which is used in the further analyses. A detailed discussion of this method is available in Mishra et al. (2024).

Appendix A.2: Rotational profile estimates for different initial guesses.

The entire analysis was re-run with different initial values from Poljančič Beljan et al. (2017); Ruždjak et al. (2004) and compared with the original analysis, where initial values were taken from Jha et al. (2021) to see if the initial guesses contributed to any significant change in the rotational profiles thus obtained. As can be seen in Fig. A.2, all the rotational profiles obtained overlap and there is no significant change even when the initial guesses obtained from the three depicted studies vary significantly (see Table A.1).

⁴ This analysis is performed using `correl_images.pro` available in the SolarSoftWare library in Interactive Data Language (IDL)

Table A.1. Rotation parameters for entire span of Nobeyama 17 GHz data obtained using different initial guesses from different studies.

Initial Values from	$A \pm \Delta A$ (°/day)	$B \pm \Delta B$ (°/day)	$C \pm \Delta C$ (°/day)
Poljančič Beljan et al. (2017)	14.523 ± 0.007	-1.37 ± 0.11	-0.20 ± 0.29
Ruždjak et al. (2017)	14.519 ± 0.007	-1.37 ± 0.11	-0.25 ± 0.29
Jha et al. (2021)	14.520 ± 0.006	-1.44 ± 0.10	-0.43 ± 0.27

Appendix A.3: Segmenting large-scale features

To accentuate the understanding of the contribution of different features at different temperatures (or heights), an image segmentation method based on adaptive intensity thresholding was designed for the bright regions (e.g, active regions) (T1 and T2 in Fig. A.1). This was achieved by using the mean method for adaptive thresholding (Chatterjee et al. 2016) to a smoothed and histogram-equalized image⁵ and is given by:

$$I_{ij} = \begin{cases} 1, & \text{if } I_{ij} \geq (\mu_{Disc} + k \sigma_{Disc}) \\ 0, & \text{otherwise} \end{cases} \quad (\text{A.1})$$

where I_{ij} is the intensity value of the ij^{th} pixel, μ_{disc} is the mean, σ_{disc} is the standard deviation of the solar disc and k ($= 1$, here) is a scalar that can be adjusted based on the attribute we aim to segment. This method segments even small-scale brightenings which might correspond to coronal hole regions as well. An additional area threshold of 120.6 arcsec^2 ($\approx 63.38 \times 10^6 \text{ km}^2$), determined using trial-and-error method, was applied to discard any spurious brightening that might be of non-physical origin and extract large-scale features that remained for the exemplar latitudinal bin.

Appendix B: Rotation parameters of different parts and features of the solar atmosphere compiled from relevant studies

⁵ The generalized code is available for open source use at <https://github.com/srinjana-routh/Bright-Regions-Nobeyama>

Table B.1. Some rotation parameters of different features and parts of the solar atmosphere as obtained through various studies. (KSO: Kanzelhoe Observatory; KoSO: Kodaikanal Solar Observatory; MWO: Mt. Wilson Observatory; White Light: WL, Debrecen Photoheliographic Data: DPD, US Air Force Solar Optical Observing Network and National Oceanic and Atmospheric Administration: NSF/NOAA)

Article	Data	$A \pm \Delta A$ (°/day)	$B \pm \Delta B$ (°/day)	$C \pm \Delta C$ (°/day)
Howard et al. (1984)	Individual Spots (MWO; 1921-1982)	14.522 ± 0.004	-2.84 ± 0.04	—
Balthasar et al. (1986)	Spot groups (MWO; 1921-1982)	14.393 ± 0.010	2.95 ± 0.09	—
	Individual Spots (GPR; 1874-1976)	14.551 ± 0.006	-2.87 ± 0.06	—
Howard et al. (1999)*	Spot groups (Uncorrected KoSO data; 1917-1985)	14.547 ± 0.005	-2.96 ± 0.05	—
	Spot groups (Uncorrected MWO data; 1917-1985)	14.459 ± 0.006	-2.99 ± 0.06	—
	Spot groups (Corrected KoSO; 1917-85)	14.461 ± 0.006	-3.02 ± 0.06	—
	Spot groups (Corrected MWO; 1917-85)	14.470 ± 0.005	-2.97 ± 0.06	—
	Individual Sunspots (Corrected MWO; 1917-85)	14.446 ± 0.003	-2.78 ± 0.03	—
	Individual Sunspots (Corrected KoSO; 1917-85)	14.456 ± 0.002	-2.88 ± 0.02	—
Gupta et al. (1999)*	Area < 5 μHem (KoSO; 1906-1987)	14.491 ± 0.003	-2.85 ± 0.03	—
	5 μHem < Area < 15 μHem (KoSO)	14.380 ± 0.004	-2.84 ± 0.04	—
	Area > 15 μHem (KoSO)	14.279 ± 0.005	-2.83 ± 0.04	—
	Area < 5 μHem (MWO; 1917-1985)	14.477 ± 0.003	-2.80 ± 0.03	—
	5 μHem < Area < 15 μHem (MWO)	14.363 ± 0.006	-2.65 ± 0.05	—
	Area > 15 μHem (MWO)	14.248 ± 0.009	-2.61 ± 0.09	—
Poljančič Beljan et al. (2017)	Spot groups (KSO sunspot drawings and WL images; 1964-2016)	14.47 ± 0.01	-2.66 ± 0.10	—
		14.50 ± 0.01	-2.87 ± 0.12	—
Ruždjak et al. (2017)*	Individual Spots (GPR; 1874-1976)	14.528 ± 0.006	-2.77 ± 0.05	—
	Individual Spots (USF/NOAA; 1977 – 2016)	14.44 ± 0.01	-2.54 ± 0.08	—
	Individual Spots (DPD; 1977 – 2016)	14.433 ± 0.009	-2.44 ± 0.08	—
	Individual Spots (GPR+USF/NOAA; 1874 – 2016)	14.501 ± 0.005	-2.71 ± 0.05	—
	Individual Spots (GPR+DPD; 1874 – 2016)	14.483 ± 0.005	-2.67 ± 0.05	—
Jha et al. (2021)*	Binary masks of sunspots (KoSO; 1923-2011)	14.381 ± 0.004	-2.72 ± 0.04	—
Mishra et al. (2024)	Ca II K (KoSO; 1907-2007)	14.61 ± 0.04	-2.18 ± 0.37	-1.10 ± 0.61
	304 Å (SDO/AIA; 2010-2023)	14.574 ± 0.012	-1.52 ± 0.12	-2.29 ± 0.22
	1600 Å	14.485 ± 0.024	-1.61 ± 0.24	-2.68 ± 0.45
	131 Å	14.649 ± 0.014	-1.33 ± 0.20	-2.99 ± 0.52
	171 Å	14.574 ± 0.032	-1.36 ± 0.29	-2.65 ± 0.46
	193 Å	14.645 ± 0.039	-0.92 ± 0.34	-2.70 ± 0.56
	211 Å	14.613 ± 0.042	-0.50 ± 0.37	-3.31 ± 0.60
	335 Å	14.656 ± 0.015	-0.96 ± 0.22	-2.75 ± 0.60

*Denotes the studies depicted in Fig. 3.